ELSEVIER

International Journal of Solids and Structures 41 (2004) 3353–3377

INTERNATIONAL JOURNAL OF SOLIDS and STRUCTURES

www.elsevier.com/locate/ijsolstr

Deformation-induced folding systems in thin-walled monolithic hexagonal metallic honeycomb

Dirk Mohr, Mulalo Doyoyo *

Impact and Crashworthiness Laboratory, Massachusetts Institute of Technology, Rm 5–222, 77 Massachusetts Avenue, Cambridge, MA 02139, USA

Received in revised form 15 December 2003

Available online 3 March 2004

Abstract

Metallic honeycombs exhibit microstructural heterogeneity under large deformation which presents a challenge to the development of mechanical models of the material using classical continuum mechanics. In order to gain insight on this problem, numerical multiaxial experiments are performed on a virtual honeycomb specimen (VHS). This involves a detailed finite element model that represents the plate-like honeycomb microstructure with three-dimensional shell elements obeying an elastic–plastic constitutive law. The VHS is subjected to large combined compressive and shear loading along its tubular direction in displacement-controlled simulations under quasi-static conditions. The observed deformation mechanisms that include plastic collapse and the formation of folding systems are analyzed at the microstructural level and their effects on the mechanical responses at the macroscopic level are discussed in-depth. Mathematical expressions of the characteristics of the folding systems, namely: folding planes, folding directions, hinge line orientations, and compatibility zones are developed and used to determine representative measures of microstructural deformation. An elliptic macroscopic plastic collapse envelope of the honeycomb is analytically and numerically evaluated, while closed-form expressions of compressive and shear strengths are presented. A linear crushing envelope defines the post-collapse behavior. The direction of inelastic deformation is found to be parallel to that of the macroscopic compressive principal stress. This study reveals that the constitutive behavior of metallic honeycombs beyond the elastic regime is controlled by folding systems.

Keywords: Honeycomb; Finite elements; Multiaxial crushing; Constitutive model; Multiaxial testing; Honeycomb plasticity; Folding systems

1. Introduction

Honeycombs are composed of a network of joined parallel tubes. The mechanical properties of a honeycomb depend on the geometry of the cross-section of the elementary tube, its base material and the

* Corresponding author. Tel./fax: +1-617-523-0371.
E-mail address: doyoyo@mit.edu (M. Doyoyo).

0020-7683/$ - see front matter © 2004 Elsevier Ltd. All rights reserved.
doi:10.1016/j.ijsolstr.2004.01.014

joining technique employed. Here, we focus on thin-walled hexagonal metallic honeycomb. That is, the elementary tubes have a hexagonal cross-section with cell walls made of a thin metallic foil.

When investigating the mechanical behavior of a honeycomb, it is useful to distinguish between the microstructural and macroscopic levels. At the microstructural level, we consider the discrete cellular structure of a honeycomb and discuss its deformation patterns and the stress distribution within the cell walls. At the macroscopic level, we consider the honeycomb as a homogeneous fictitious material, where the response is described in terms of macroscopic stresses and strains. Various relationships between microstructural and macroscopic properties have been established in the past. Examples are the macroscopic elastic moduli that may be directly determined from the Young's modulus of the cell wall material and the specific cell wall geometry. A comprehensive summary on the mechanical properties of honeycombs is given in the textbook by Gibson and Ashby (1997).

Not much is known about the response of a metallic honeycomb to large out-of-plane loading. This type of loading involves a combination of normal and shear loading along the tubular direction of the honeycomb. It is typical for honeycombs because they are frequently used as core materials in sandwich structures. Experiments on aluminum honeycomb reveal the highly complex microstructural processes governing the mechanical response: formation of elastic buckles, plastic collapse of cell walls, evolution of deformation-induced imperfection fields, propagation and nucleation of plastic hinge lines, stretching and folding of cell walls (Doyoyo and Mohr, 2003; Mohr and Doyoyo, 2003, 2004). Finite element simulations of the microstructural response of a honeycomb have proven to be a powerful means to investigate the mechanical behavior of cellular materials. Grediac (1993) studied the height dependency of the shear modulus using a three-dimensional finite element model of a honeycomb cell; Xu and Qiao (2002) employed a periodic unit cell finite element model in their study on the skin effect. The dynamic in-plane response of elastic–viscoplastic polycarbonate honeycomb was modeled by Papka and Kyriakides (1999) using two-dimensional beam models. This modeling technique was later adopted by Hönig and Stronge (2002) to study the effect of local inertia in aluminum honeycomb at high strain rates.

Here, we go one step further and perform a non-linear three-dimensional finite element analysis of a honeycomb microstructure. Our objective is to gain further insight on the deformation mechanisms at the microstructural level as large macroscopic out-of-plane displacements are applied. The core of the present study is the 'virtual honeycomb specimen (VHS)' that represents the honeycomb microstructure discretized by 3D-shell elements with an elastic–plastic constitutive law. The simulations represent the biaxial testing of a honeycomb in its sandwich configuration. Displacement-controlled simulations are performed for various combinations of normal and shear loading. The results reveal that the cell walls of the honeycomb microstructure fold in deformation-induced folding systems. The three characteristics (i) folding plane, (ii) folding direction and (iii) hinge line orientation are identified for various folding systems. At the macroscopic level, an elliptic plastic collapse initiation envelope is found along with a linear post-collapse envelope that characterizes the crushing regime.

2. Virtual experiments

2.1. Material

The microstructural geometry and cell wall material properties of the VHS are chosen according to a standard commercial honeycomb. The characteristic cross-section of the honeycomb is shown schematically in Fig. 1(a). It has a hexagonal cellular microstructure with a wall thickness of $t = 33$ μm, an expansion angle of $\theta = 40°$, cell wall widths $l = 3.1$ mm and $h = 2.4$ mm, and a relative density of $\rho/\rho_0 = 1.8\%$. The width to thickness ratios of the cell walls are $l/t \approx 94$ and $h/t \approx 73$ for the

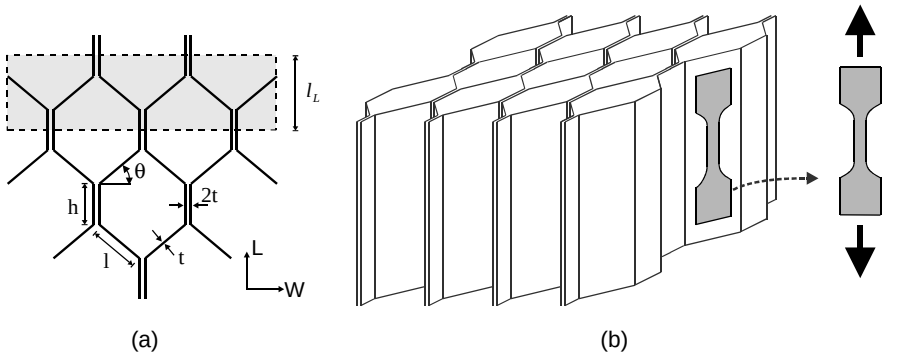

Fig. 1. (a) Honeycomb geometry in the L–W-plane; the dashed rectangle shows a part of the microstructure that is represented in the VHS; (b) extraction of a microtensile dogbone specimen from the honeycomb microstructure.

single-thickness walls, and $l/2t \approx 47$ and $h/2t \approx 36$ for the double-thickness walls. Dogbone specimens with a gage width of 1 mm are extracted from the cell walls of a real honeycomb (Fig. 1(b)) and tested in a force-controlled microtensile testing device (Gudlavalleti, 2002). The cell wall material (aluminum 5056-H39 foil) exhibited an ideal plastic response at a constant engineering stress of $\tilde{\sigma}_y = 265$ MPa; fracture occurred at an engineering strain of about 8% (Ames, 2003).

2.2. Specimen

Fig. 2(a) shows the section of the honeycomb microstructure represented by the VHS. The VHS was $l_W = 38$ mm wide and $C = 7.5$ mm high, which corresponded to a width to height ratio of $l_W/C = 5$. We make use of the microstructural periodicity along the L-direction and restrict our model to a representative band of width $l_L = h + l\sin\theta = 4.4$ mm along the L-direction (Figs. 1(a) and 2(a)). Symmetric boundary conditions are applied to the boundaries in the L-direction (Fig. 3(b)), which, at the macroscopic level, may be interpreted as a plane strain condition along the L-direction. All degrees of freedom are restricted at the bottom of the specimen, whereas a homogeneous displacement field (u_W, u_T) is prescribed at the top boundary (Fig. 3(a)).

The width to height ratio affects the overall homogeneity of the stress field along the W-direction. This ratio should be as large as possible. The results of simulations using larger specimens (e.g. $l_W = 76$ mm)

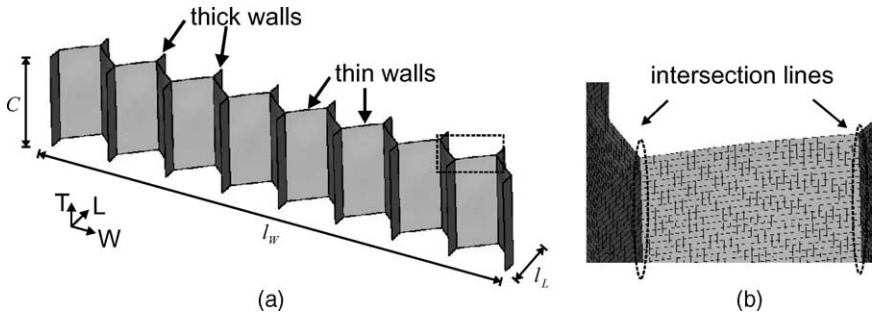

Fig. 2. (a) Schematic of the microstructure of the VHS; the thick walls are aligned with the L-direction; (b) details of the FE-discretization with shell elements; the intersection between the flat walls is labeled as 'intersection line'.

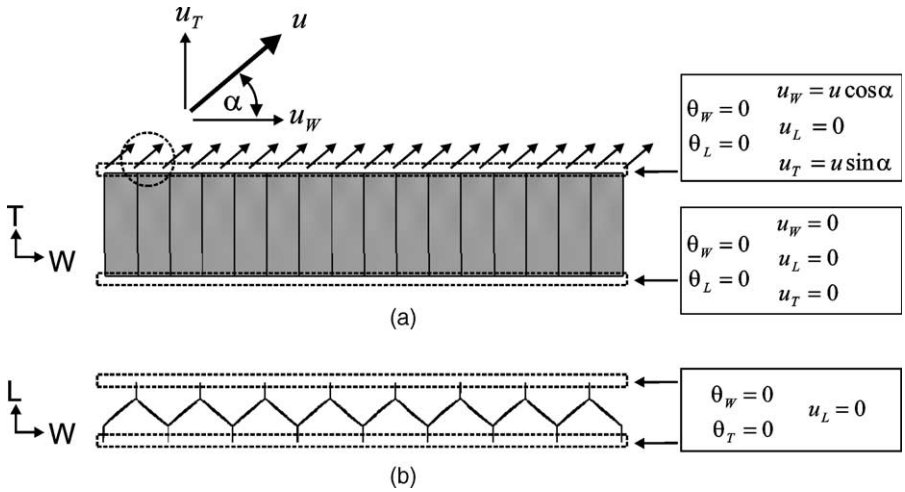

Fig. 3. Boundary conditions of the FE-model of the VHS. θ_i and u_i denote the rotational and translational degrees of freedom of the shell element in the global coordinate system respectively: (a) side view, (b) top view.

showed the same deformation mechanisms as those of the present specimen. The quantitative effect on the macroscopic stress levels was typically less than 5%. The choice of the specimen height has an influence on the macroscopic strains defined below, which results in a size dependency of the normalized response curves. An investigation of this effect is left to future studies. The present specimen height is chosen such that the governing deformation mechanisms observed are representative of honeycomb specimens with $C > 7.5$ mm.

2.2.1. Details of the FE-model

(i) Spatial discretization of cell wall geometry with 53,700 four-node shell elements (Belytschko-Tsay formulation, reduced in-plane integration, 5 integration points through cell wall thickness, active hourglass control); this corresponded to an average element side length of 0.1 mm (see detail in Fig. 2(b)); the mesh of the perfect cell wall geometry is generated using the HYPERMESH preprocessing software. Next, the shape functions of the lowest elastic buckling mode under compressive loading are computed with ABAQUS/standard (Abaqus, 1999). Based on the shape of this buckling mode, an 'imperfect mesh' is generated and used for the subsequent non-linear analysis. The initial imperfections introduced are of the order of the cell wall thickness.

(ii) Explicit time integration of the non-linear problem using the LS-DYNA v960 solver (Hallquist, 1999); by means of automatic density scaling, 200,000 constant time steps of $\Delta t = 2.5$ ns are performed to linearly apply a total displacement of $u = -5$ mm under a predefined loading angle α (Fig. 3(a)); problem time and time step are carefully chosen such as to guarantee quasi-static loading conditions. This requirement is verified at the macroscopic level by ensuring the kinetic energy to be small as compared to the strain energy.

(iii) The cell wall material is represented by a phenomenological J_2-plasticity model with multilinear isotropic hardening.

(iv) Penalty formulation for possible cell wall contact; the shell thickness is considered for contact, but thickness changes are neglected.

(v) The resultant force vs. problem time signals at frequencies above 4000 Hz are cut-off using a standard SAE-filter.

2.2.2. Limitations

Besides well-known limitations of the mathematical model and its finite element solution, two physical limitations shall be noted:

(i) The double-thickness cell walls in a real honeycomb are typically made of two single-thickness cell walls that are bonded together. Thus, given the finite strength of the thin adhesive bond in a real honeycomb, total or partial delamination may occur between adjacent cell walls. However, due to the lack of reliable modeling technique for delamination, simulations are carried out for a monolithic honeycomb, where the double-thickness walls are represented by a single shell element layer of double thickness.
(ii) Cell wall fracture is not included in the model.

2.3. Experimental program

Simulations are performed under various loading conditions. The combined normal and shear displacement loading on the top boundary is characterized by the biaxial loading angle α and the resultant displacement u (Fig. 3(a)). With the exception of the simulation for 'pure shear' loading, the biaxial loading angle is kept constant for individual simulations while a maximum resultant displacement of $u = -5$ mm is applied. In terms of normal and shear displacements, u_T and u_W, we have:

$$u_T = u \sin \alpha, \tag{1}$$

$$u_W = u \cos \alpha. \tag{2}$$

Furthermore, we introduce the macroscopic normal and shear strains, ε and γ, by normalizing the displacements with respect to the specimen height C:

$$\varepsilon = \frac{u_T}{C}, \tag{3}$$

$$\gamma = \frac{u_W}{C}. \tag{4}$$

The macroscopic strain path is linear and defined by the tangent of the biaxial loading angle: $\varepsilon = \gamma \tan \alpha$. Displacement-controlled simulations are performed for biaxial loading angles of 0°, 10°, 20°, 30°,40°, 50°, 60°, 70°, 80° and 90°. The corresponding strain paths are shown in Fig. 4.

The resultant force components acting on the top boundary, F_W and F_T, were written as ascii output from each simulation. The macroscopic shear and normal stresses τ and σ are calculated from the total forces that act on the specimen:

$$\sigma = \frac{F_T}{A_0}, \tag{5}$$

$$\tau = \frac{F_W}{A_0}, \tag{6}$$

where $A_0 = l_W l_L$ is the cross-sectional area of the VHS. Under pure shear loading, we apply the shear displacement along the W-direction and impose the force boundary condition $F_T = 0$ along the T-direction. As a result, a non-linear strain path is observed (Fig. 4).

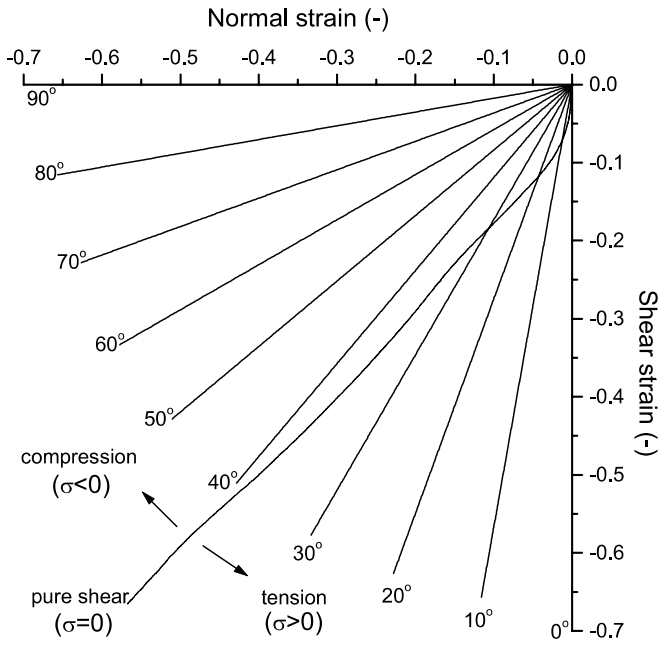

Fig. 4. Strain paths for the biaxial numerical experiment on the VHS.

3. Results and analysis

3.1. Overview

A summary of all normal stress vs. normal strain curves and all shear stress vs. shear strain curves is given in Figs. 5 and 6, respectively. The curves are remarkably similar to previous experimental results (Mohr and Doyoyo, 2004). A pronounced initial peak stress is observed in the normal stress–strain curves, denoting plastic collapse of the microstructure. After initial collapse, the following observations are noteworthy:

(i) All curves are in hierarchical order: with the exception of the results for pure shear, neither the normal nor the shear stress–strain curves intersect. From small to large loading angles, the normal stress level increases, whereas the shear stress level decreases.
(ii) Macroscopic tensile stresses develop for loading angles below 40° (Fig. 5). This may be explained by Fig. 4. The curve for pure shear represents the strain path for $\sigma = 0$. As a first approximation, tensile stresses develop when the magnitude of the compressive normal strain applied is smaller than the corresponding normal strain for pure shear.
(iii) As normal tensile stresses develop, the corresponding shear stress–strain curves typically exhibit significant hardening (see 0°, 10°, 20°, 30° in Fig. 6).
(iv) The curve for pure shear shows a more or less constant stress level (Fig. 6). It separates the shear stress–strain curves into two groups: Those comprising strain hardening lie above; the curves for large loading angles ($\alpha > 40°$) lie below.
(v) For large loading angles and large normal strains ($\varepsilon < -0.1$), an almost constant plateau stress is observed in the normal stress–strain curves. This regime is labeled 'crushing' in Fig. 5.

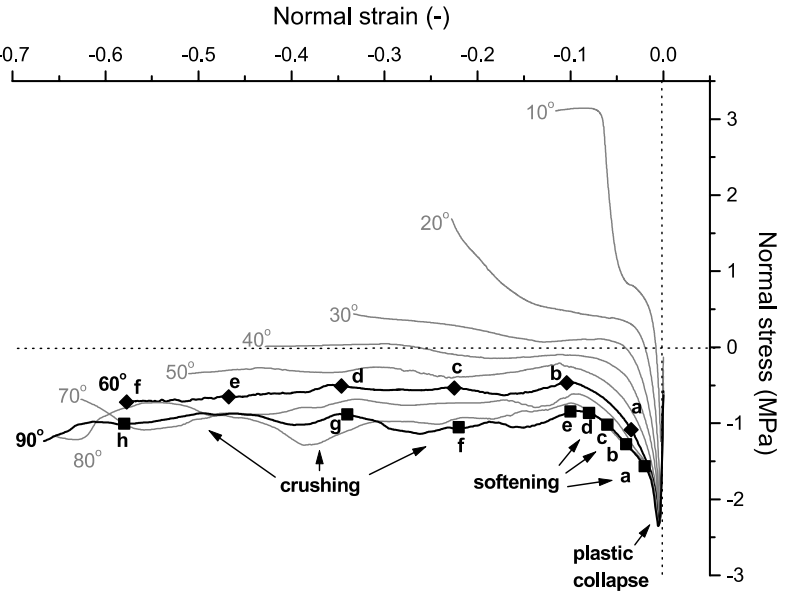

Fig. 5. Macroscopic normal stress–strain curves at different loading angles.

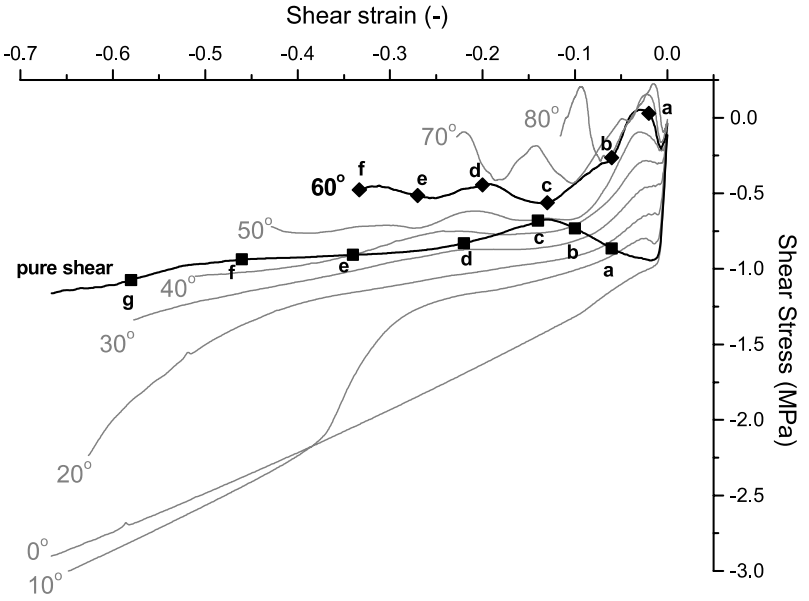

Fig. 6. Macroscopic shear stress–strain curves at different loading angles.

In the present study, we focus on the behavior under combined compressive and shear stresses with practical applications in mind. For clarity of our discussion, we emphasize the naming of the different parts of the honeycomb microstructure (Fig. 2): The single-thickness walls are referred to as *thin walls*, the

double-thickness walls, all aligned in L-direction, are referred to as *thick walls*. The line joint between thick and thin walls is called the *intersection line*. Among the output quantities at the microstructural level, we frequently refer to the *internal energy density*. The internal energy density represents the plastic dissipation per unit volume in a shell element. By contrast to strain or stress components, it is calculated as the mean over the volume of the shell element and thus, independent of the shell thickness coordinate. As a reference, the value of internal energy density at 8% axial strain during uniaxial compression of Al5056-H39 is 21.2 mJ/mm^3 which corresponds to a specific energy absorption of 7.8 J/g (which is calculated as the internal energy density divided by the mass density of the cell wall material).

3.2. Onset of plastic collapse

With the exception of 0° loading, all macroscopic normal stress–strain curves show a monotonically increasing macroscopic stress until a pronounced peak stress is reached and the stress level drops. We labeled this point as 'plastic collapse' in Fig. 5. Careful examination of the von Mises stress distribution in the mid-plane of the thin cell walls provides further insight (Fig. 7(a)–(f)).

Under uniaxial compression, the maximum peak load is reached as plastic yield occurs along the intersection lines (Fig. 7(f)), depicting the von Kármán theory of the strength of thin plates under load (von Kármán et al., 1932). Prior to plastic collapse, elastic buckles form and grow in the honeycomb microstructure, which results in the unloading of cell wall centers and the concentration of stress at the intersection lines. Note from Fig. 7(f) that the membrane stresses are almost zero in the center of the deflected cell walls, whereas the yield stress ($\tilde{\sigma}_y = 265$ MPa) is exceeded at the intersection line.

For pure shear loading, the microstructural stress distribution prior to collapse is fairly uniform (Fig. 7(a)) confirming the derivations by Kelsey et al. (1958). In terms of principal stresses, a state of pure shear can be transformed into a state of combined compressive and tensile stresses of equal magnitudes. However, after elastic buckling, the thin walls are relieved of the compressive principal stress, while the compressive principal stress in the thick walls increases. The difference, as compared to the von Kármán mechanism under uniaxial compression, is that the buckling-related microstructural load-redistribution occurs from thin walls to thick walls rather than from wall center to the intersection lines. As a result, the stress state in the buckled thin walls under macroscopic pure shear loading is almost free of stress concentrations. Microstructural yield occurs first within a narrow band, but the stress level in the entire thin walls is close to yield (Fig. 7(a)).

Fig. 7 also shows the von Mises stress distribution for other loading angles. Clearly, transition from a shear-type homogeneous collapse mechanism to a normal loading dominated non-homogeneous von Kármán collapse mechanism is observed.

3.3. Softening regime: folding system activation

Beyond the initial peak in the macroscopic stress–strain curves, a pronounced softening regime is observed. Fig. 8 shows a sequence of deformed microstructures that are observed during this regime for 90° loading. As outlined by McFarland (1963), the monolithic thin-walled honeycomb microstructure develops folds to accommodate the applied macroscopic displacement. The development of the first fold takes place in the softening regime, which leads to the activation of so-called 'folding systems' (Mohr and Doyoyo, 2004). Folding systems are composed of plastic hinge lines and compatibility zones that allow for the kinematically admissible folding of the honeycomb microstructure. Hinge lines and compatibility zones have been highlighted in Fig. 8. Compatibility zones are located at the intersection lines where the kinematic compatibility of adjacent folding systems is achieved at the expense of plastic stretching or compression of the cell walls. Observe that the plastic dissipation per unit volume is significantly higher within the compatibility zones than along the plastic hinge lines. The end of the softening regime is reached as cell

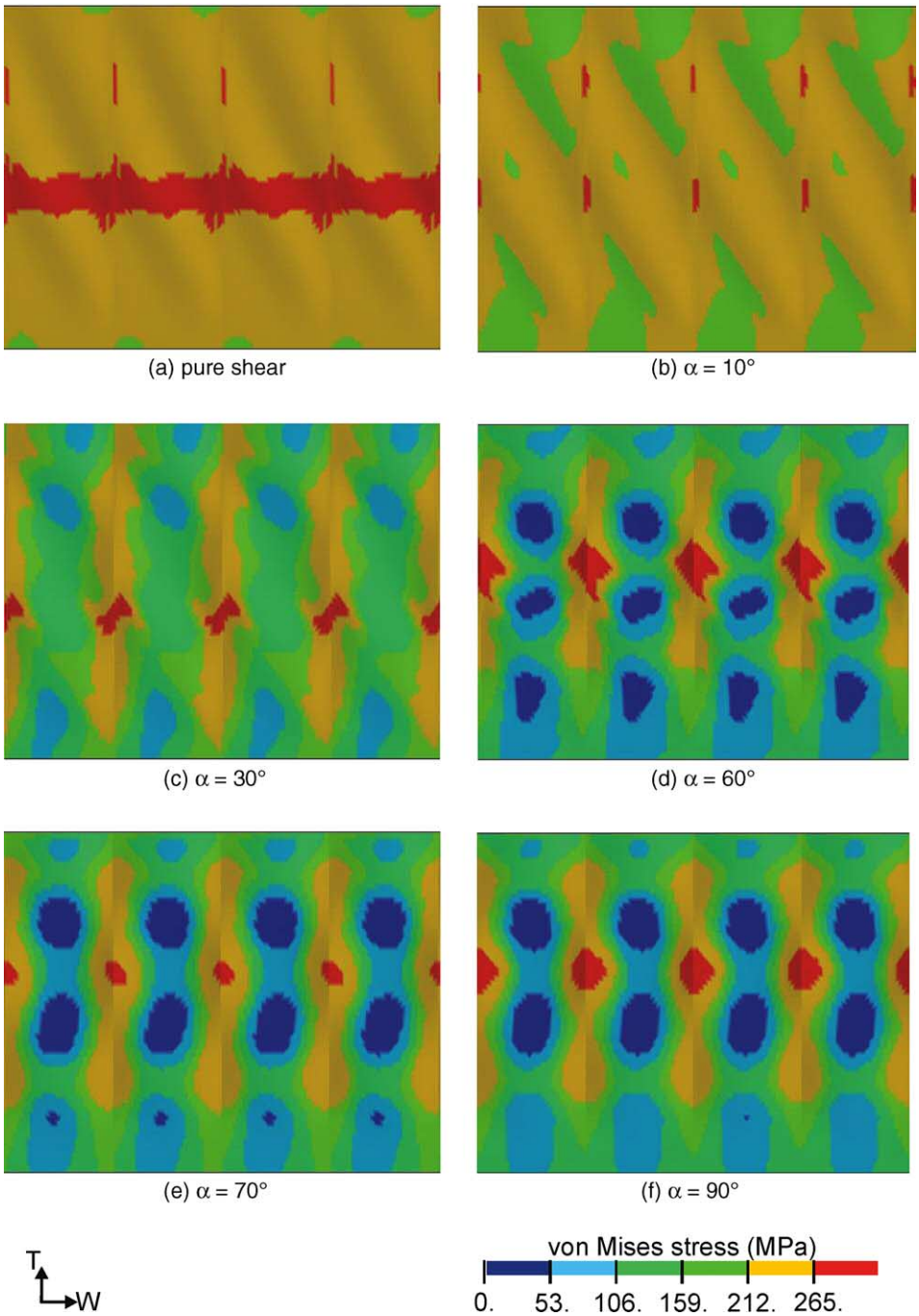

Fig. 7. Contour plot of the von Mises stress in the shell mid-plane of the thin walls at the onset of plastic collapse. Note that the yield stress of the cell wall material is $\bar{\sigma}_y = 265$ MPa.

wall contact occurs in the compatibility zones, increasing the load carrying capacity (Fig. 8(d)). At this point, the thick walls underwent a 90° rotation around the L-axis (Fig. 8(d)).

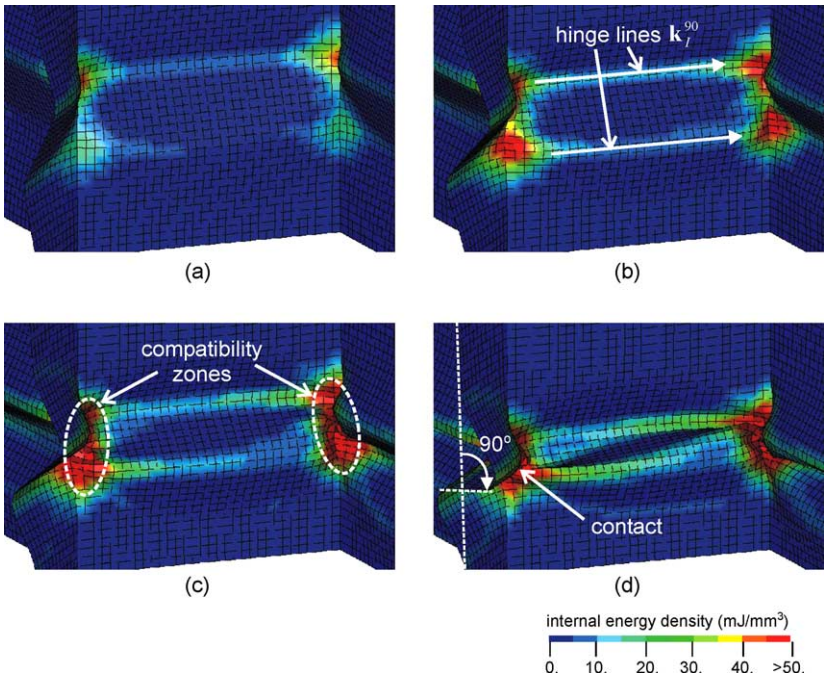

Fig. 8. Formation of the first fold during 90° loading: (a) $u = -0.15$ mm [a], (b) $u = -0.3$ mm [b], (c) $u = -0.45$ mm [c] and (d) $u = -0.6$ mm [d]. The letter in square brackets denotes the data point on the 90°-stress–strain curve in Fig. 5.

The development of folds is the natural response of prismatic thin-walled structures to large compressive loads. Compressive stresses concentrate along the intersection lines where the structural deflection of the thin cell walls is prohibited by the lateral support of the adjacent cell walls. In the center of a cell wall however, large deflections occur and the remaining membrane stress state is predominantly that of uniaxial tension. To illustrate, the membrane stress state in the mid-plane of the cell walls is visualized by the vector field of the principal stresses in each four-node element (Fig. 9(a)). Clearly, the stress state corresponds to uniaxial tension along the hinge lines, with the maximum principal stress acting perpendicular to the bending direction. This stress component is due to the circumferential stretching associated with the deflection. The region between the two hinge lines is almost free of stress, whereas compressive stresses are observed in the highly deformed compatibility zones. Similar observations are made for various combinations of combined macroscopic compressive and shear loading. The main difference is the orientation of the hinge lines within a folding system.

Consider the limiting case of pure shear next. The schematic in Fig. 10 shows a possible mechanism for pure shear deformation. According to this mechanism, the thick cell walls are bent without any stretching whereas the thin walls are bent and sheared at the same time (Fig. 10(b)). However, as discussed above, in terms of principal stresses, shearing of a thin-wall by itself also implies compression and thus causes the formation of folds. Fig. 11 shows the sequence of deformed microstructures in the softening regime for pure shear. Dashed lines are used to establish the link to the schematic in Fig. 10. Initially, local shear buckles emerge (Fig 11(a)), then transform into deeper shear folds (Fig. 11(b) and (c)) until they become dominant and determine the characteristic hinge lines of the folding system for pure shear loading (Fig. 11(d)). Cell wall contact occurs at the end of the softening regime. The principal stress state corresponding to configuration (c) is shown in Fig. 9(b). Even more dramatically than during 90°-loading, the membrane stress

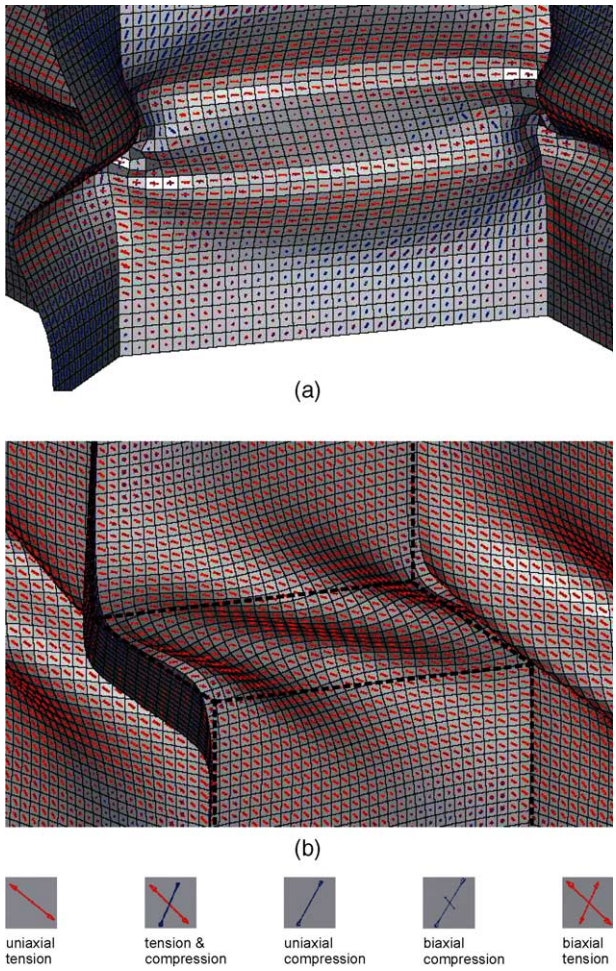

Fig. 9. Principal stress states in the shell mid-surface: (a) at $u = -0.45$ mm during 90° loading, (b) at $u = -1.05$ mm during pure shear loading.

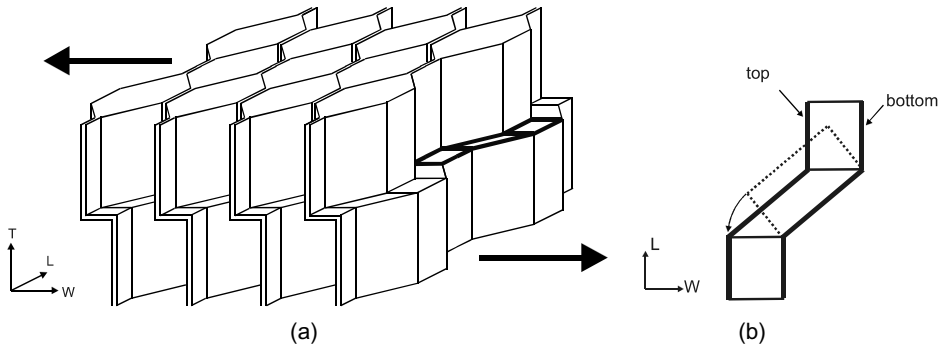

Fig. 10. A schematic of the shear mechanism (a) 3D view, (b) view from the top of the view in (a). The dashed rectangle shows the shape of the thin wall after bending without shearing.

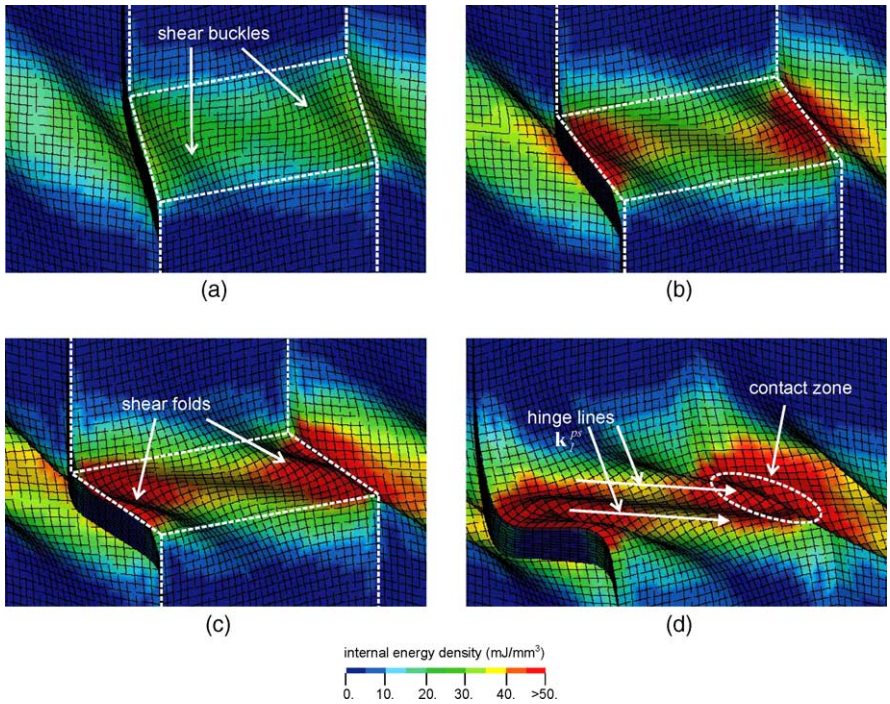

Fig. 11. Formation of the first fold during pure shear loading: (a) $u = -0.45$ mm [a], (b) $u = -0.75$ mm [b], (c) $u = -1.05$ mm [c], and (d) $u = -1.65$ mm [d]. The letter in square brackets denotes the data point on the stress–strain curve for pure shear in Fig. 6.

state in the mid-plane is characterized by uniaxial tension parallel to the hinge lines. Furthermore, note that according to the schematic in Fig. 10(b), it is the diagonal of the conceptually sheared cell wall that experiences the largest stretch. Consequently, the hinge lines are more or less parallel to this diagonal (Fig. 11(c)).

The microstructural behavior in the softening regime during 50°, 60°, 70° and 80° loading may be explained by the same mechanisms. The major difference is the orientation of the hinge lines within the characteristic folding system. Fig. 12 shows the formation of the first fold during 60° loading. Note that the upper hinge line is inclined at a well-defined angle with respect to the W–L-plane, but still parallel to the most stretched fiber in the folding microstructure.

3.4. Crushing regime: progressive folding

Progressive folding is the dominant microstructural deformation mechanism in the crushing regime. At the same time, the macroscopic stress fluctuates around an almost constant stress level. The progressive folding of honeycombs under uniaxial compression was investigated by various authors and is well understood (McFarland, 1963; Wierzbicki, 1983). With the formation of the first layer of folds, significant imperfections emerge in the vicinity of the first fold (Mohr and Doyoyo, 2003). As a result, the activation threshold for subsequent folds is reduced, which allows for the formation of subsequent folds at a stress level below the initial collapse stress. Fig. 13 illustrates a side view of progressive folding under uniaxial compression. Note the intense localization of deformation within the microstructure. The honeycomb folds layer by layer, thereby transforming the microstructure from its uncrushed configuration to its crushed

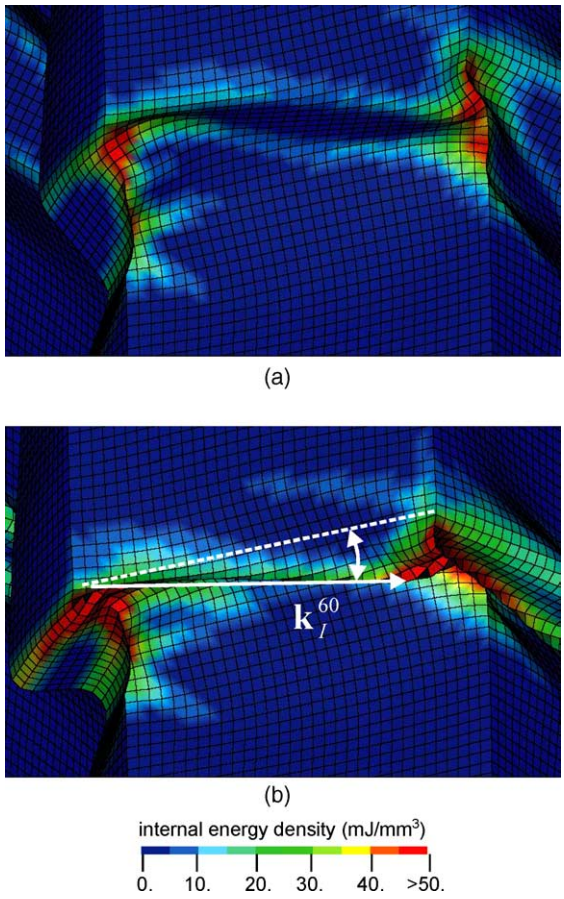

Fig. 12. Formation of the first fold during 60° loading: (a) $u = -0.3$ mm [a], and (b) $u = -0.9$ mm [b]. The letter in square brackets denotes the data point on the stress–strain curves for 60° loading in Figs. 5 and 6.

configuration. During 90° loading, the folds pile up along the T-direction. A vertical cut through the deformed thin walls confirms this observation (Fig. 16(f)).

Fig. 14(a) shows the deforming microstructure at the end of the softening regime in pure shear. In the figure, the first column is a 3D-view while the second column is the side view of the deforming microstructure. Similarly to the 90° results, the energy dissipation is highly localized within a narrow band in the microstructure. As anticipated in the mechanism drawn in Fig. 10(a), the top and bottom behave rigidly and move relative to each other while the microstructure is highly deformed within the localization band. In the crushing regime, two additional folds form almost simultaneously above and below the first fold (Fig. 14(b)–(d)). At this time, the width of the localization band increases. In other words, the microstructure is transformed from uncrushed to crushed state. The corresponding cut through the thin walls of the deformed microstructure reveals the regular folding pattern in pure shear (Fig. 16(a)). As compared to 90°, the folds are not piled up along the T-direction but accumulated at a much lower angle. Furthermore, note that the folds are three-dimensionally arranged in space and do not touch in the cutting plane (Fig. 16(a)). In a typical side view (second column in Fig. 14), only one fold is seen.

A series of pictures from the 60° simulation shows progressive folding under combined loading. Again, only one fold is seen from the side (second column in Fig. 15), but the three folds become visible in the

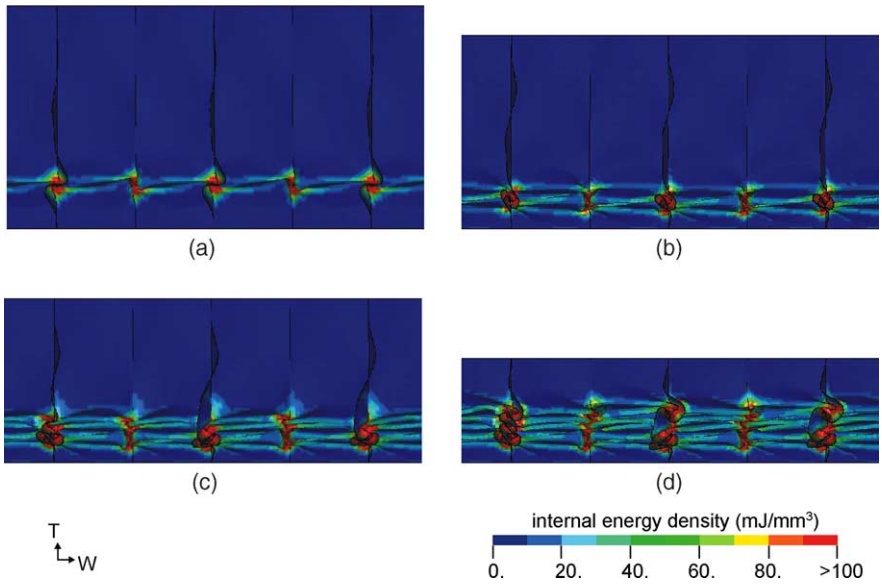

Fig. 13. Deformed microstructure during 90° loading: (a) $u = -0.75$ mm [e], (b) $u = -1.65$ mm [f], (c) $u = -2.55$ mm [g], and (d) $u = -4.35$ mm [h]. The letter in square brackets denotes the data point on the stress–strain curve for pure shear in Fig. 5.

3D-view (first column in Fig. 15). Cuts through the deformed microstructures at $u = -5$ mm after loading along various stress paths is presented in Fig. 16. A series of folds is typically aligned along a characteristic direction. It must be noted that this direction is not monotonically related to the biaxial loading angle. A full sequence of the cuts throughout loading under 70° is shown in Fig. 17. The first complete fold grows along the T-direction (Fig. 17(b) and (c)), but rotates during the formation of the subsequent fold (Fig. 17(c)–(e)) until it reaches its final position aligned with the other folds.

4. Microstructural folding systems

It transpires from the simulation results that the honeycomb microstructure deforms progressively producing a regular folding pattern. Furthermore, it is observed that deformation localizes within the honeycomb microstructure. Rather than forming a homogeneously deformed microstructure, two distinct configurations emerge in the honeycomb microstructure: uncrushed and crushed configurations. The crushed configuration includes the folded cell walls, whereas the uncrushed configuration preserves the initial tubular microstructure. The transition from uncrushed to crushed configuration is controlled by the deformation-induced folding systems in the honeycomb microstructure. Microstructural folding systems are defined as follows.

4.1. Definition

Consider a schematic of the microstructural deformation mechanism under combined loading (Fig. 18). The top and bottom part of the microstructure are both uncrushed and move relative to each other. At the same time, the microstructure between the top and the bottom is crushed. Recall that an undeformed honeycomb is composed of three types of cell walls that may be distinguished in the W–L-plane (Fig. 1(a)): a thin wall aligned at an angle $\theta_1 = \theta$ with respect to the W-direction (type I), a thin wall aligned at an angle

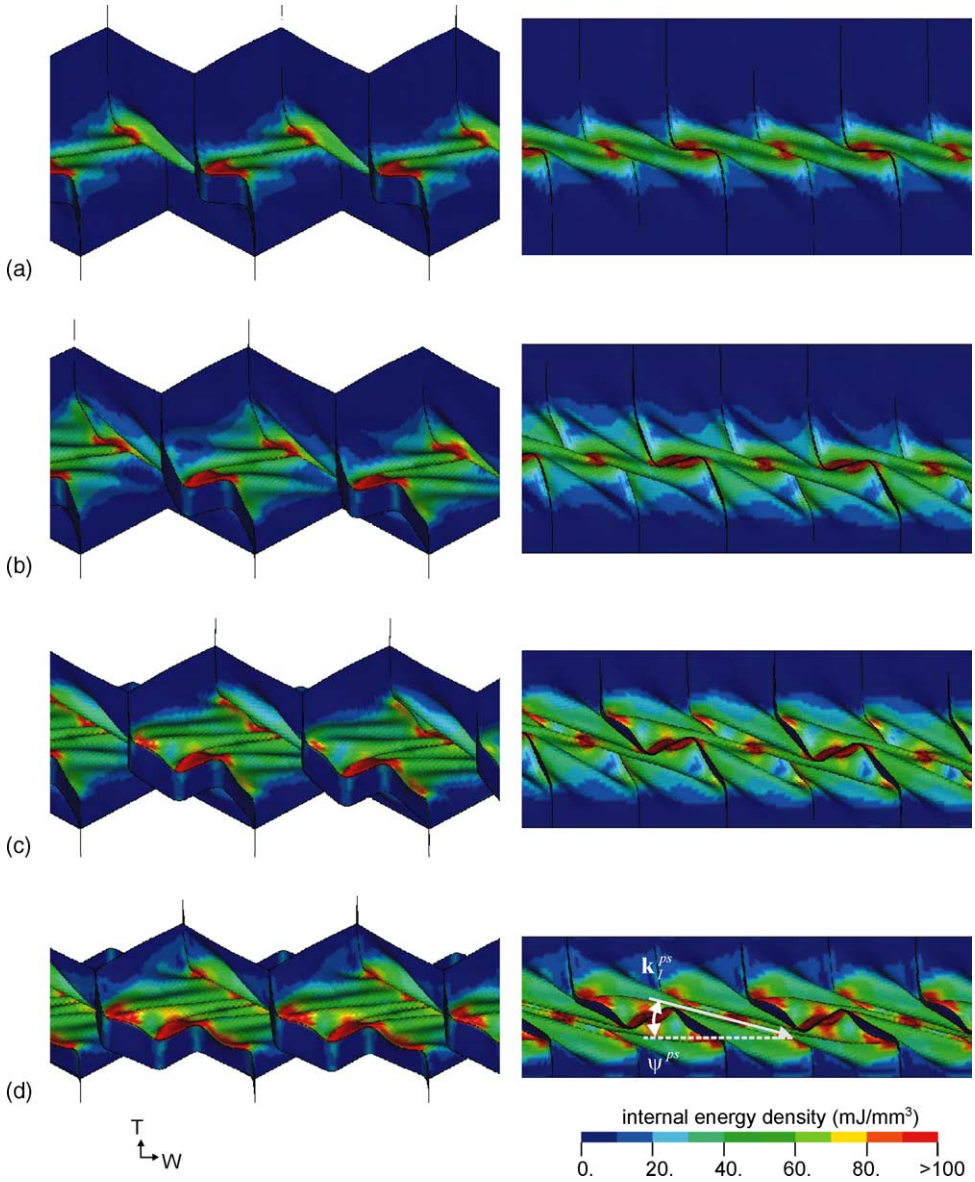

Fig. 14. Deformed microstructure during pure shear loading: (a) $u = -1.65$ mm [d], (b) $u = -2.55$ mm [e], (c) $u = -3.45$ mm [f], and (d) $u = -4.35$ mm [g]. The letter in square brackets denotes the data point on the stress–strain curve for pure shear in Fig. 6. In this figure, the first column is a 3D-view while the second column is the side view of the microstructure.

$\theta_{II} = \pi - \theta$ with respect to the W-direction (type II), and a thick wall aligned with the L-direction (type III). It is postulated that the transformation of an individual cell wall from uncrushed to crushed configuration is controlled by an associated folding system. Consider the transformation of a type I cell wall (labeled 'I' in Fig. 18(c)). The corresponding folding system is shown in Fig. 19(b). Three attributes define the folding system:

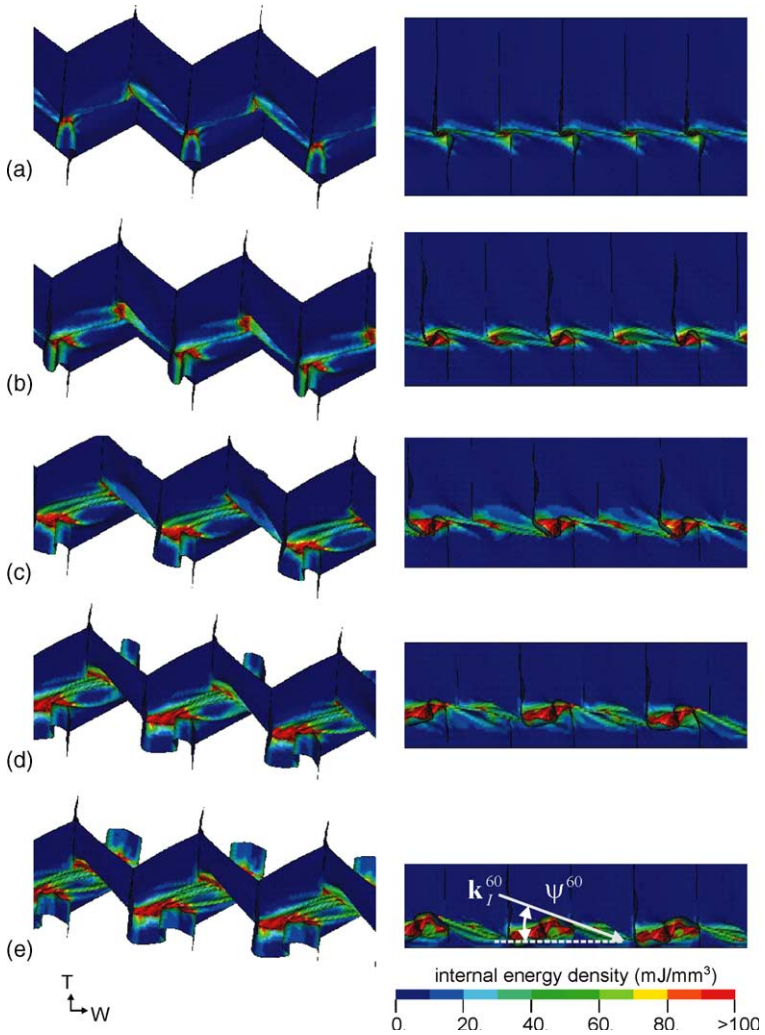

Fig. 15. Deformed microstructure during 60° loading: (a) $u = -0.9$ mm [b], (b) $u = -1.95$ mm [c], (c) $u = -3.0$ mm [d], (d) $u = -4.05$ mm [e], and (e) $u = -5.0$ mm [f]. The letter in square brackets denotes the data point on the stress–strain curve for pure shear in Figs. 5 and 6. In this figure, the first column is a 3D-view while the second column is the side view of the microstructure.

(i) the *folding plane* that contains the folds, mathematically described by its normal vector $\mathbf{n}_i^\alpha$,
(ii) the *folding direction* $\mathbf{m}_i^\alpha$ that determines the direction of fold alignment in the T–W-plane, and
(iii) the *hinge line orientation*, represented by the vector $\mathbf{k}_i^\alpha$.

In the above representation, the superscript $(\cdot)^\alpha$ emphasizes the dependence of a folding system on the loading angle, whereas the subscript $(\cdot)_i$, $i = \mathrm{I}, \mathrm{II}, \mathrm{III}$ accounts for the type of cell wall. In other words, folding systems are defined with respect to the macroscopic loading direction and with respect to the cell wall structure. Furthermore, in analogy with crystal plasticity, we may formally introduce the Burger's vector of a folding system: $\mathbf{b}^\alpha = \lambda_i^\alpha \mathbf{m}_i^\alpha$, where λ_i^α denotes the folding wavelength as shown in Fig. 19(b).

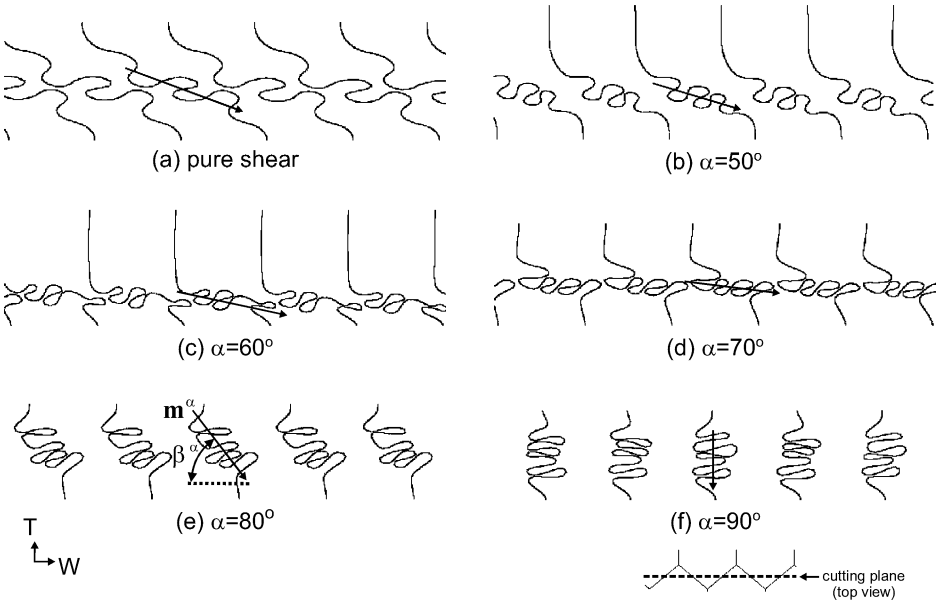

Fig. 16. Cuts through the folding microstructure in the T–W-plane for various loading angles at $u = -5$ mm. The vector denotes the folding direction.

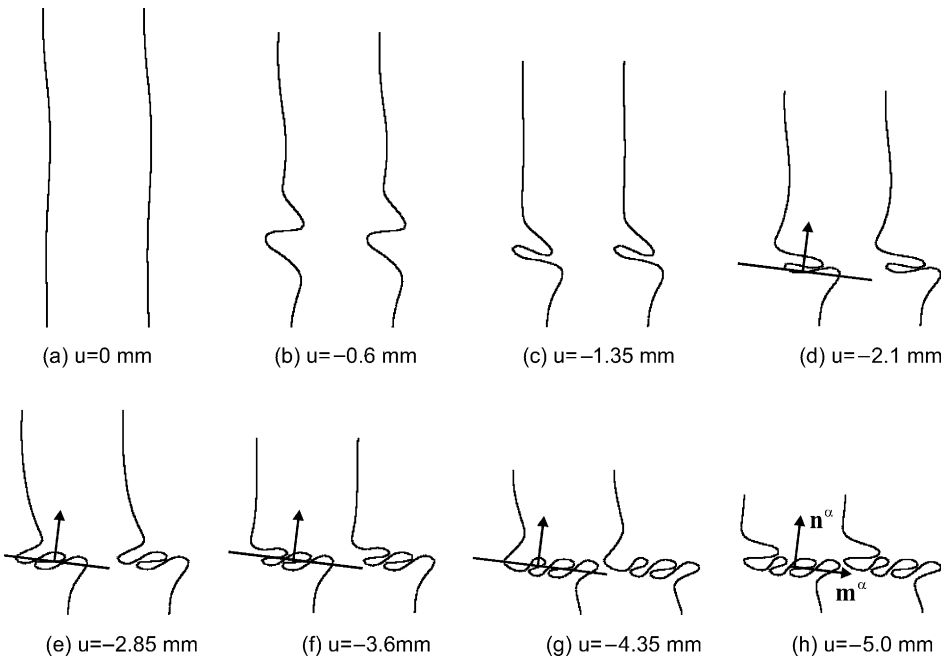

Fig. 17. Cuts through the folding microstructure in the T–W-plane during 70° loading. The normal to the folding plane and the folding direction are shown in (h).

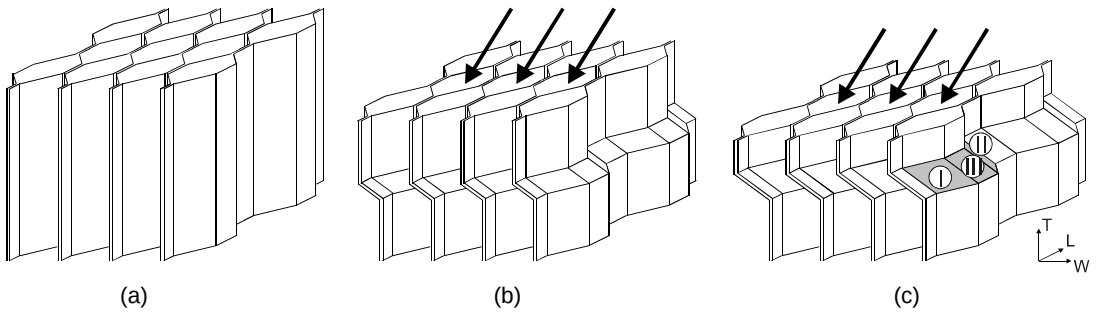

Fig. 18. Folding mechanism during combined loading.

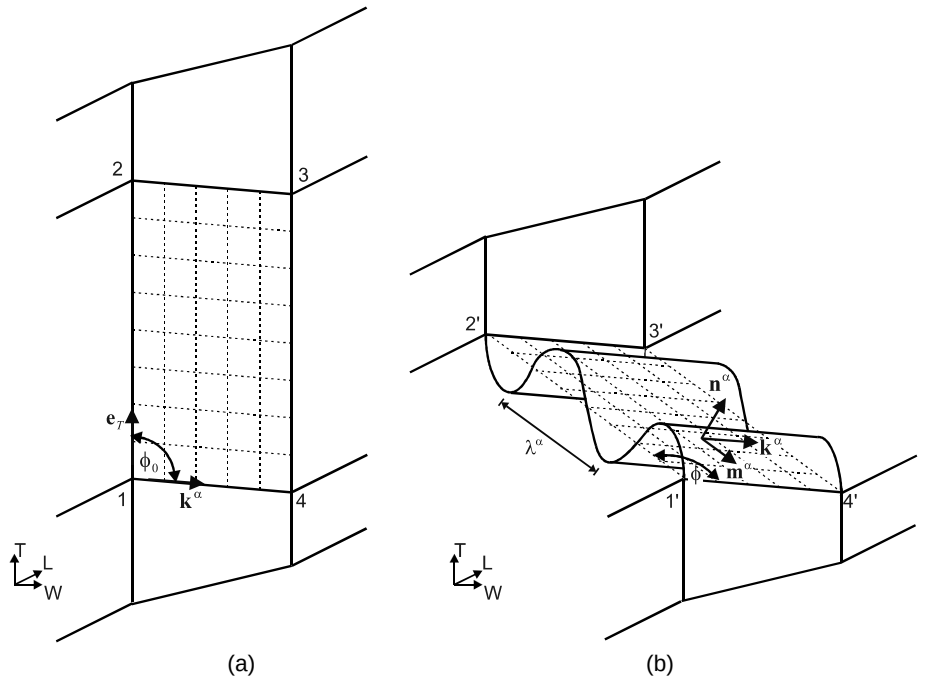

Fig. 19. Microstructural folding system: (a) initial configuration, (b) intermediate configuration.

4.2. Evaluation

The folding systems are identified during pure shear, 50°, 60°, 70°, 80° and 90° loading. First, we focus on the folding systems for cell walls of type I. The vectors $(\mathbf{e}_W, \mathbf{e}_L, \mathbf{e}_T)$ aligned with the initial orthotropic axes of the honeycomb microstructure provide the vector basis for the algebraic expressions developed below. From the cuts through the folded thin walls in the T–W-plane (Fig. 16), we find $[\mathbf{m}^\alpha_{\mathrm{I}}]_T = -[\mathbf{m}^\alpha_{\mathrm{I}}]_W \tan\beta^\alpha$ (the square bracket with subscript denotes the component of a vector); the angle β^α is defined in Figs. 16(e) and 20(b) as the angle between the folding direction and the W–L-plane. Thus, the vector indicating the folding direction reads

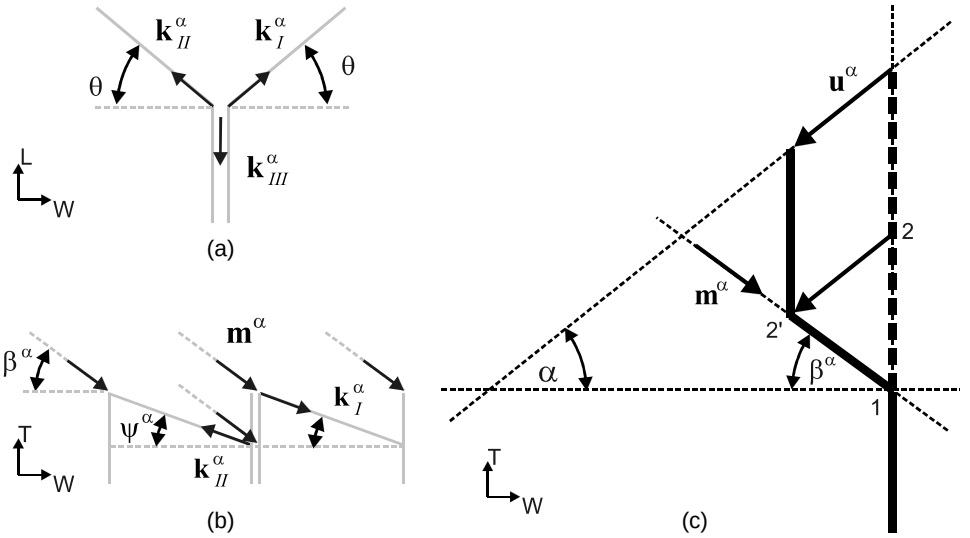

Fig. 20. Kinematics in a folding system.

$$\mathbf{m}^{\alpha}_{\mathrm{I}} = \cos\beta^{\alpha}\mathbf{e}_W - \sin\beta^{\alpha}\mathbf{e}_T. \tag{7}$$

Next, consider the projections of the vector $\mathbf{k}^{\alpha}_{\mathrm{I}}$ on the same plane (e.g. Figs. 14(d) and 15(e)). Here, we have $[\mathbf{k}^{\alpha}_{\mathrm{I}}]_T = -[\mathbf{k}^{\alpha}_{\mathrm{I}}]_W \tan\psi^{\alpha}$ as can be seen in Fig. 20(b). Furthermore, the projection on the L–W-plane requires $[\mathbf{k}^{\alpha}_{\mathrm{I}}]_L = [\mathbf{k}^{\alpha}_{\mathrm{I}}]_W \tan\theta$ (Fig. 20(a)). Thus, we have

$$\mathbf{k}^{\alpha}_{\mathrm{I}} = \frac{\mathbf{e}_W + \tan\theta\mathbf{e}_L - \tan\psi^{\alpha}\mathbf{e}_T}{\sqrt{1+\tan^2\theta+\tan^2\psi^{\alpha}}}. \tag{8}$$

Since both unit vectors, $\mathbf{m}^{\alpha}_i$ and $\mathbf{k}^{\alpha}_i$, are situated in the folding plane, we can calculate the normal vector:

$$\mathbf{n}^{\alpha}_i = \frac{\mathbf{m}^{\alpha}_i \times \mathbf{k}^{\alpha}_i}{\|\mathbf{m}^{\alpha}_i \times \mathbf{k}^{\alpha}_i\|}. \tag{9}$$

The measurements of the angles β^{α} and ψ^{α} along with the components of the vectors $\mathbf{m}^{\alpha}_{\mathrm{I}}$, $\mathbf{k}^{\alpha}_{\mathrm{I}}$, and $\mathbf{n}^{\alpha}_{\mathrm{I}}$ for the folding systems of type I cell walls are summarized in Table 1. For the folding systems of type II cell walls, we have

Table 1
Measurements of parameters in the folding systems for type I cell walls

α[°]	β [°]	ψ [°]	$[\mathbf{k}^{\alpha}]_W$	$[\mathbf{k}^{\alpha}]_L$	$[\mathbf{k}^{\alpha}]_T$	$[\mathbf{m}^{\alpha}]_W$	$[\mathbf{m}^{\alpha}]_L$	$[\mathbf{m}^{\alpha}]_T$	$[\mathbf{n}^{\alpha}]_W$	$[\mathbf{n}^{\alpha}]_L$	$[\mathbf{n}^{\alpha}]_T$	E^{α}_{mm}	E^{α}_{mk}
Pure shear[a]	20	12	0.76	0.63	−0.16	0.94	0.00	−0.34	0.34	−0.17	0.93	−0.22	−0.30
50	17	12	0.76	0.63	−0.16	0.96	0.00	−0.29	0.29	−0.11	0.95	−0.30	−0.30
60	12	20	0.74	0.62	−0.27	0.98	0.00	−0.21	0.20	0.17	0.96	−0.47	−0.25
70	7	20	0.74	0.62	−0.27	0.99	0.00	−0.12	0.12	0.27	0.95	−0.65	−0.24
80	52	10	0.76	0.64	−0.13	0.62	0.00	−0.79	0.61	−0.63	0.48	−0.77	−0.21
90	90	0	0.77	0.64	0.00	0.00	0.00	−1.00	0.64	−0.77	0.00	−1.00	0.00

[a] $\alpha = 45°$ assumed for kinematic evaluation.

$$\begin{aligned}\mathbf{m}^{\alpha}_{\mathrm{II}} &= \mathbf{m}^{\alpha}_{\mathrm{I}},\\ \mathbf{k}^{\alpha}_{\mathrm{II}} &= -[\mathbf{k}^{\alpha}_{\mathrm{I}}]_W\mathbf{e}_W + [\mathbf{k}^{\alpha}_{\mathrm{I}}]_L\mathbf{e}_L - [\mathbf{k}^{\alpha}_{\mathrm{I}}]_T\mathbf{e}_T,\\ \mathbf{n}^{\alpha}_{\mathrm{II}} &= [\mathbf{n}^{\alpha}_{\mathrm{I}}]_W\mathbf{e}_W - [\mathbf{n}^{\alpha}_{\mathrm{I}}]_L\mathbf{e}_L + [\mathbf{n}^{\alpha}_{\mathrm{I}}]_T\mathbf{e}_T.\end{aligned} \tag{10}$$

And finally, for the thick cell walls (type III), we have

$$\begin{aligned}\mathbf{m}^{\alpha}_{\mathrm{III}} &= \mathbf{m}^{\alpha}_{\mathrm{I}},\\ \mathbf{k}^{\alpha}_{\mathrm{III}} &= -\mathbf{e}_L,\\ \mathbf{n}^{\alpha}_{\mathrm{III}} &= -[\mathbf{m}^{\alpha}_{\mathrm{I}}]_T\mathbf{e}_W - [\mathbf{n}^{\alpha}_{\mathrm{I}}]_W\mathbf{e}_T.\end{aligned} \tag{11}$$

To quantify the deformation in a folding system, we introduce the measures $[E^{\alpha}_i]_{mm}$ and $[E^{\alpha}_i]_{mk}$ for the compressive and shear deformation in a folding system, respectively. First, we calculate the change of length of the line 1–2 (Fig. 19). Upon evaluation of the kinematic relationships in the T–W-plane (Fig. 20(c)), we can express the relative change of length as

$$[E^{\alpha}_{\mathrm{I}}]_{mm} = \frac{1}{\cos\beta^{\alpha}(\tan\beta^{\alpha} + \tan\alpha)} - 1. \tag{12}$$

To measure the shear deformation, we consider the change of the angle ϕ between the hinge line orientation and the folding direction. In the undeformed configuration, the angle ϕ_0 (between points 2, 1, and 4 in Fig. 19(a)) is given by

$$\cos\phi_0 = \mathbf{k}^{\alpha}\mathbf{e}_T, \tag{13}$$

whereas for the angle ϕ in the deformed configuration (between points 2′, 1′, and 4′ in Fig. 19(b)), we have:

$$\cos\phi = -\mathbf{m}^{\alpha}\mathbf{k}^{\alpha}, \tag{14}$$

which allows us to introduce the measure for shear deformation as

$$[E^{\alpha}_{\mathrm{I}}]_{mk} = \frac{1}{2}\cos\left(\frac{\phi}{\phi_0}\frac{\pi}{2}\right). \tag{15}$$

For the remaining folding systems, we have $[E^{\alpha}_{\mathrm{I}}]_{mm} = [E^{\alpha}_{\mathrm{II}}]_{mm} = [E^{\alpha}_{\mathrm{III}}]_{mm}$, $[E^{\alpha}_{\mathrm{I}}]_{mk} = [E^{\alpha}_{\mathrm{II}}]_{mk}$ and $[E^{\alpha}_{\mathrm{III}}]_{mk} = 0$. The last two columns in Table 1 show the measures of the compressive and shear deformation in the folding system for type I cell walls. It indicates that the shear deformation within the folding systems decreases as the biaxial loading angle increases, while the normal deformation increases. The relationship between the above microstructural deformation measurements and the macroscopic displacement $\mathbf{u}$ can be obtained by integrating $[E^{\alpha}_i]_{mm}$ along the folding direction $\mathbf{m}^{\alpha}_i$ (Mohr and Doyoyo, 2003).

5. Phenomenology at the macroscopic level

The introduction of folding systems provides a basis for the formulation of mechanism-based constitutive models that shall be developed in the future. At this stage, we determine two phenomenological envelopes that characterize the macroscopic inelastic response in the normal-shear stress plane.

5.1. Plastic collapse envelope

Recall from our analysis above that elastic buckling dramatically changes the stress distribution in the cellular honeycomb microstructure and thereby reduces its load carrying capacity. Before we determine the collapse envelope from a fit to our data, we calculate the theoretical yield envelope assuming perfectly flat

cell walls. Let the stress state in the thin cell walls (or the microscopic stress state) and the macroscopic stress state be denoted by $(\tilde{\sigma}, \tilde{\tau})$ and (σ, τ), respectively. Following Kelsey et al. (1958), by assuming a uniform stress distribution in the honeycomb cell walls, we can relate the microscopic and macroscopic stresses in the elastic regime as:

$$\frac{\tilde{\sigma}}{\sigma} = \frac{\left(\frac{h}{l} + \sin\theta\right)\frac{l}{t}\cos\theta}{2\frac{h}{l} + 1}, \tag{16}$$

$$\frac{\tilde{\tau}}{\tau} = \frac{h}{t} + \frac{l}{t}\sin\theta. \tag{17}$$

For the present honeycomb, we have $\tilde{\sigma}/\sigma \cong 40$ and $\tilde{\tau}/\tau \cong 133$. Note that the von Mises yield condition applies at the microstructural level, so that the microscopic yield surface is $\sqrt{\tilde{\sigma}^2 + 3\tilde{\tau}^2} - \tilde{\sigma}_y = 0$. Substituting Eqs. (16) and (17) into the yield condition, we obtain the macroscopic yield envelope:

$$f_0 = \left(\frac{\sigma}{\sigma_0}\right)^2 + \left(\frac{\tau}{\tau_0}\right)^2 - 1 = 0, \tag{18}$$

where σ_0 is the macroscopic yield stress under uniaxial compression and τ_0 is the macroscopic yield stress under pure shear:

$$\sigma_0 = \frac{\left(2\frac{h}{l} + 1\right)\tilde{\sigma}_y}{\left(\frac{h}{l} + \sin\theta\right)\frac{l}{t}\cos\theta} \tag{19}$$

and

$$\tau_0 = \frac{\tilde{\sigma}_y}{\sqrt{3}\left(\frac{h}{t} + \frac{l}{t}\sin\theta\right)}. \tag{20}$$

Upon evaluation of Eqs. (19) and (20) for the present honeycomb, we find $\sigma_0 = 6.6$ MPa and $\tau_0 = 1.15$ MPa. However, the fit of Eq. (18) in the simulation data qualitatively conforms with the elliptic nature of the data points at the onset of plastic collapse (see Fig. 21), but the magnitudes of the theoretical yield stresses are higher. From a fit of Eq. (18) into the simulation data, we find $\sigma_0 = 2.9$ MPa and $\tau_0 = 0.93$ MPa. (Aside: The simulation data points at plastic collapse were determined as the initial peak stresses from the unfiltered force-time curves. This improves the accuracy of the measurements, while at the same time it explains some minor difference in magnitude between the peaks shown in Figs. 5, 6 and 21.) The deviation from the analytical predictions demonstrates the impact of microstructural failure, particularly under uniaxial compression. In the case of pure shear, microstructural buckling has only little influence on the size of the elastic domain and Eq. (20) is a reasonable estimate of the macroscopic shear strength. However, the microstructural load-redistribution under uniaxial compression (discussed in detail in the previous section), reduces the maximum load carrying capacity by a factor of 2.

A better analytical expression for the macroscopic yield stress under uniaxial compression is obtained by applying the von Kármán model to a honeycomb. Closely following von Kármán's derivation (von Kármán et al., 1932), Mohr and Doyoyo (2003) found the following expression for the macroscopic peak stress under uniaxial compression:

$$\sigma_0 = \frac{3\pi}{\sqrt{3(1-\nu_s^2)}} \frac{\sqrt{E_s\tilde{\sigma}_y}t^2}{l\cos\theta(h + l\sin\theta)}, \tag{21}$$

where $\nu_s = 0.33$ denotes the elastic Poisson's ratio and $E_s = 72$ GPa the Young's modulus of the cell wall material, respectively. Upon evaluation, we find $\sigma_0 = 2.6$ MPa which is close to 2.9 MPa from the simulation.

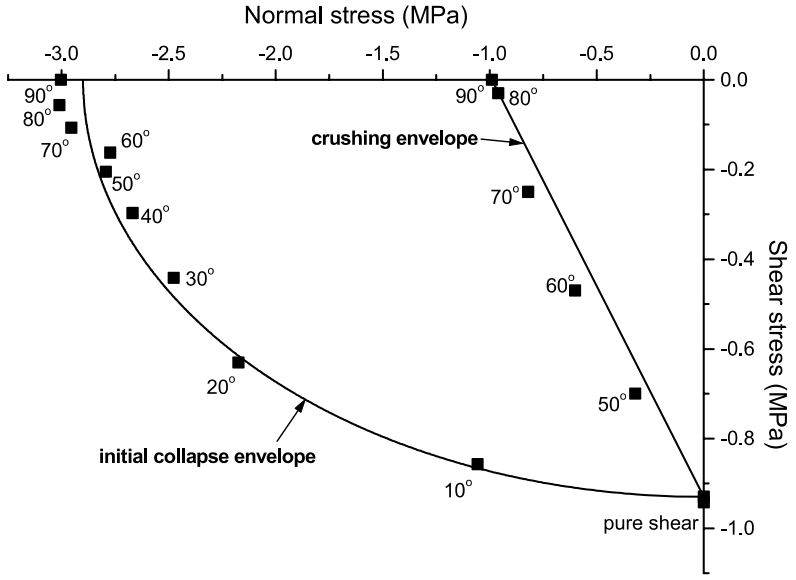

Fig. 21. Characteristic envelopes in the macroscopic shear stress vs. compressive stress plane.

5.2. Crushing regime

The concept of a 'crushing envelope' was introduced to describe the behavior under combined compressive and shear stresses (Mohr and Doyoyo, 2004). Based on the experimental observation of an approximately constant stress level in the crushing regime, the macroscopic plateau stresses $\bar{\sigma}$ and $\bar{\tau}$ are defined as

$$\bar{\sigma} = \frac{1}{\varepsilon_{\max} - \varepsilon^*} \int_{\varepsilon^*}^{\varepsilon_{\max}} \sigma \, \mathrm{d}\varepsilon \tag{22}$$

and

$$\bar{\tau} = \frac{1}{\gamma_{\max} - \gamma^*} \int_{\gamma^*}^{\gamma_{\max}} \tau \, \mathrm{d}\gamma, \tag{23}$$

where the intervals $[\varepsilon^*, \varepsilon_{\max}]$ and $[\gamma^*, \gamma_{\max}] = \tan\alpha^{-1}[\varepsilon^*, \varepsilon_{\max}]$ represent the length of the crushing regime. The present observation of folding systems in the honeycomb microstructure provides an important argument as to why both the shear and normal stress levels are roughly constant in the crushing regime: the folding system that is formed during the softening regime is determined by the biaxial loading angle and hence, as the biaxial loading angle is kept constant, subsequent folds form in the same folding plane, along the same folding direction and at the same folding wavelength. In other words, the crushing of the microstructure is a recurring process and thus, the macroscopic stress response is theoretically periodic over a characteristic interval $\Delta\varepsilon$. This characteristic interval may be identified for selected stress–strain curves, but as a first approximation for the mean stress over the interval $\Delta\varepsilon$, we integrate along the full strain path in the crushing regime.

According to our analysis of the stress–strain curves, the crushing regime begins as the compressive stress reaches its minimum in the softening regime. Based on the results shown in Fig. 5, we chose $\varepsilon^* = -0.1$ and $\varepsilon_{\max} = u_{\max}\sin\alpha$. (Note that a densification regime follows the crushing regime; however, the densification regime was not yet reached at the maximum displacement applied in the present simulations.) The corre-

sponding plot of the plateau stress data points $(\bar{\sigma}, \bar{\tau})$ is shown in Fig. 21. The straight line in Fig. 21 shows the crushing envelope, defined as

$$f_c(\bar{\sigma}, \bar{\tau}) = \frac{\bar{\sigma}}{\bar{\sigma}_0} + \frac{\left|\bar{\tau}\right|}{\bar{\tau}_0} - 1 = 0. \tag{24}$$

From a fit to the data, we find $\bar{\sigma}_0 = -0.99$ MPa for the plateau stress under uniaxial compression and $\bar{\tau}_0 = 0.93$ MPa for the plateau stress under pure shear.

Next, we suggest a simple expression to describe the relationship between the strain and stress increments in the crushing regime. The simulations for pure shear indicated that the corresponding strain path is fairly parallel to the strain trajectory for $\alpha = 45°$ (Fig. 4). In other words, the direction of the strain increment $d\varepsilon/d\gamma$ appears to be close to the direction of the compressive principal macroscopic plateau stress. For a macroscopic stress state of combined compression and shear, we have for the angle χ between the W-axis and the direction of the compressive principal stress:

$$\frac{\pi}{4} \leqslant \chi \leqslant \frac{\pi}{2}, \quad \bar{\sigma} < 0: \quad \tan 2\chi = \frac{2\left|\bar{\tau}\right|}{\bar{\sigma}}. \tag{25}$$

Our hypothesis for the direction of the strain increment reads:

$$d\varepsilon < 0: \quad \tan \chi = -\frac{|d\gamma|}{d\varepsilon} = \tan \alpha \tag{26}$$

We tested this hypothesis for other loading angles and found reasonable agreements (Table 2). After combining Eqs. (25) and (26), we get the following relationship:

$$\xi < 0: \quad \frac{d\varepsilon}{d\gamma} = \frac{-2\,\mathrm{sign}(\tau)}{\sqrt{4 + \xi^2} - \xi}, \tag{27}$$

where $\xi = \bar{\sigma}/|\bar{\tau}|$ denotes the compressive-shear stress ratio in the crushing regime.

6. Comment about the significance of the compatibility zones

The deformation fields in folding systems must satisfy kinematic compatibility with adjacent folding systems. As a result, characteristic compatibility zones form. Fig. 22 shows two neighboring type I and type II folding systems in the T–W-plane. The biaxial loading angle was $\alpha = 70°$. The configuration corresponds to $u = -5$ mm, but the microstructural displacements were scaled by a factor of 0.5 to make the presentation more clear. Also, the thick cell walls are not shown. The vertical dashed lines highlight the deformed intersection lines. Furthermore, we encircled the compatibility zone (labeled CZ 1-2) between the folding systems (labeled FS-1 and FS-2). With the distance from its boundaries, the microstructural deformation field in the compatibility zones changes from a plastic bending-dominated regular folding pattern to a membrane-dominated state of stretched and sheared cell walls. Note from the contour plot that this

Table 2
Direction of strain increment

α[°]	45[a]	50	60	70	80	90
χ[°]	45.0	51.4	61.3	74.3	88.2	90.0

The upper row shows the biaxial loading angle α, whereas the angle χ in the lower row indicates the direction of the minimum principal macroscopic stress in the crushing regime (both with respect to the W-axis).

[a] $\alpha = 45°$ assumed for pure shear.

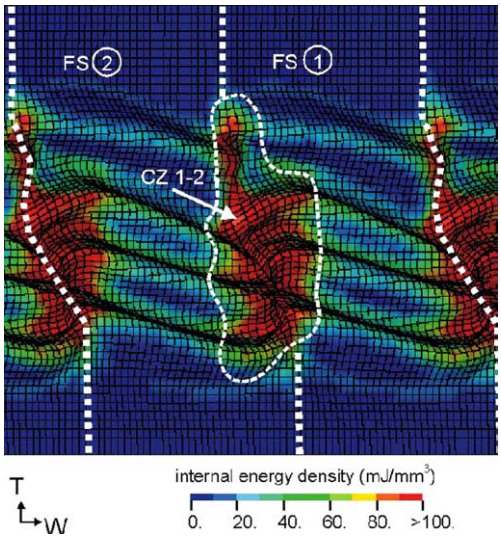

Fig. 22. Compatibility zone (CZ) between two adjacent folding systems (FS). Nodal displacements were scaled by a factor of 0.5 and the intersecting thick wall is not shown to improve the visualization of the folding system at $u = -5$ mm under 70°-loading. The contour plot shows the internal energy density.

transition is accompanied by a dramatic increase of internal energy density. After integrating the internal energy within the encircled area in Fig. 22, we find that the energy dissipation within the compatibility zone is about 75% of the energy dissipation in the entire folding system. We note that plastic dissipation in the compatibility zones between two folding systems i and j depends, among other variables, on the angle between the normal vectors, $\mathbf{n}_i^\alpha \mathbf{n}_j^\alpha$, and the depth of the folds along the normal direction. These variables are typically used for the analysis of the crushing mechanics of thin-walled prismatic structures under axial loading (e.g. Wierzbicki and Abramowicz, 1983). Additionally, kinematic incompatibility arises from the inclination of the hinge lines with respect to the W–L-plane. Here the jump $[u_T^\alpha] = l \tan \psi^\alpha \cos \theta$ might prove to be a useful measure (Fig. 20(b)). The in-depth analysis of the compatibility zones is left to future research. Its numerical treatment requires finer meshes along the intersection zones as well as reliable models to represent delamination between neighboring cell walls.

7. Conclusions

The detailed finite element analysis of the honeycomb microstructure under large biaxial displacement loading provides important insight into the microstructural mechanisms that determine the macroscopic behavior. This study reveals that the constitutive behavior of metallic honeycombs beyond the elastic regime is controlled by folding systems. After the plastic collapse of the elastically buckled microstructure, cell walls are progressively folded in deformation-induced folding systems. The three characteristics of folding systems—folding plane, folding direction and hinge line orientation—were identified for various biaxial loading angles. In analogy with crystal plasticity, a mathematical formalism was introduced and used to measure the localized deformation. An elliptic envelope in the macroscopic normal vs. shear stress plane describes the onset of plastic collapse, while a linear envelope characterizes the crushing regime. Furthermore, the direction of inelastic deformation is found to be parallel to the macroscopic compressive principal stress.

Acknowledgements

We thank Professor Tomasz Wierzbicki for valuable discussions. We are grateful to Nicoli Ames for performing microtensile tests at Professor Lallit Anand's Solid Mechanics and Materials Laboratory, MIT. Altair Engineering is thanked for providing a free license of HYPERMESH. Thanks are due to Livermore Software Technology Corporation (LSTC), Livermore, CA, for providing LS-DYNA and LS-POST. We acknowledge HKS, Providence, RI, for making ABAQUS/standard available under academic license. Financial support of the Joint MIT/Industry Ultralight Consortium is also acknowledged.

References

Abaqus, 1999. Reference Manuals, Providence, RI.

Ames, N.M., 2003. Private communication.

Doyoyo, M., Mohr, D., 2003. Microstructural response of aluminum honeycomb to combined out-of-plane loading. Mechanics of Materials 35 (9), 865–876.

Gudlavalleti, S., 2002. Mechanical testing of solid materials at the micro-scale, Master's Thesis, Department of Mechanical Engineering, MIT.

Gibson, L.J., Ashby, M.F., 1997. Cellular Solids: Structure and Properties, second ed. Cambridge University Press.

Grediac, M., 1993. A finite element study of the transverse shear in honeycomb cores. International Journal of Solids and Structures 30 (13), 1777–1788.

Hallquist, J.O., 1999. LS-DYNA Theoretical Manual. LSTC, Livermore, CA.

Hönig, A., Stronge, W.J., 2002. In-plane dynamic crushing of honeycomb. Part I: Crush band initiation and wave trapping. International Journal of Mechanical Sciences 44, 1665–1696.

Kelsey, S., Gellatly, R.A., Clark, B.W., 1958. The shear modulus of foil honeycomb cores. Aircraft Engineering 30, 294–302.

McFarland, R.K., 1963. Hexagonal cell structure under post-buckling axial load. AIAA Journal 1, 1380–1385.

Mohr, D., Doyoyo, M., 2003. Nucleation and propagation of plastic collapse bands in aluminum honeycomb. Journal of Applied Physics 94 (4), 2262–2270.

Mohr, D., Doyoyo, M., 2004. Experimental investigation on the plasticity of aluminum honeycomb. Journal of Applied Mechanics 71 (2).

Papka, S.D., Kyriakides, S., 1999. Biaxial crushing of honeycombs—Part II: Analysis. International Journal of Solids and Structures 36 (29), 4397–4423.

von Kármán, T., Sechler, E.E., Donnell, L.H., 1932. The strength of thin plates in compression. Transactions of ASME 54, 53–63.

Wierzbicki, T., 1983. A crushing analysis of metal honeycomb. International Journal of Impact Engineering 1, 157–174.

Wierzbicki, T., Abramowicz, W., 1983. On the crushing mechanics of thin-walled structures. Journal of Applied Mechanics 50, 727–739.

Xu, F.X., Qiao, P., 2002. Homogenized elastic properties of honeycomb sandwich with skin effect. International Journal of Solids and Structures 39 (8), 2153–2188.